

Cite this: *RSC Adv.*, 2018, 8, 18419

# Construction of g-C<sub>3</sub>N<sub>4</sub> and FeWO<sub>4</sub> Z-scheme photocatalyst: effect of contact ways on the photocatalytic performance†

Cong Wang,‡ Guanlong Wang,‡ Xiufang Zhang, \* Xiaoli Dong, Chun Ma, Xinxin Zhang, Hongchao Ma and Mang Xue

Photocatalysis has been regarded as an attractive strategy for the elimination of contaminants, but its performance is usually limited by the fast recombination of photogenerated electron–holes. A heterojunction photocatalyst could achieve the effective separation of electron–holes. However, the electrons migrate to the less negative band while holes move to the less positive band, leading to a weakened redox ability. Z-scheme photocatalysis is a feasible way to realize the efficient separation of photogenerated electron–holes without sacrificing the reductive ability of electrons and oxidative ability of holes. In this work, a new Z-scheme photocatalyst, composed of g-C<sub>3</sub>N<sub>4</sub> (photocatalyst I), FeWO<sub>4</sub> (photocatalyst II) and RGO (electron mediator), was fabricated through a facile hydrothermal and mixing method. The effect of contact ways (the electron mediator firstly combined with photocatalyst I or with photocatalyst II) on the Z-scheme photocatalytic performance was investigated. The photocatalytic removal rate of rhodamine B (RhB) was largely enhanced by the construction of a Z-scheme photocatalyst, compared with the g-C<sub>3</sub>N<sub>4</sub>/FeWO<sub>4</sub> composite without RGO. The contact ways could affect the photocatalytic ability of a Z-scheme photocatalyst. The enhanced photocatalytic performance was attributed to the Z-scheme induced efficient separation of photogenerated charge carriers. Furthermore, remaining holes (on the VB of FeWO<sub>4</sub>) or remaining electrons (on the CB of g-C<sub>3</sub>N<sub>4</sub>) with powerful oxidation or reduction ability would promote the photocatalytic degradation of RhB.

Received 3rd April 2018

Accepted 9th May 2018

DOI: 10.1039/c8ra02882f

rsc.li/rsc-advances

## 1. Introduction

Over the past few decades, semiconductor photocatalysis has been widely applied in the destruction of organic pollutants in air or water.<sup>1,2</sup> Various semiconductor materials, such as oxides,<sup>3</sup> sulfides,<sup>4</sup> nitrides,<sup>5</sup> or solid solutions,<sup>6</sup> have been exploited as single-phase photocatalysts. However, rapid recombination of the photoexcited electron–hole pairs usually occurs in single-phase photocatalysis, which will restrict the photocatalytic activity. To address this issue, composite photocatalysts are commonly used to make efficient charge carrier separation.<sup>7–10</sup> Nevertheless, photogenerated electrons in a composite photocatalysts migrate to and accumulate in less negative conduction bands, while holes migrate to and accumulate in less positive valence bands. Thus, from the point of view of thermodynamics, the oxidation performance of holes or the reduction ability of electrons is weakened compared with

single-component photocatalysts. The Z-scheme photocatalytic system, which proceeds through a two-step photoexcitation (PS II of a photocatalytic oxidation system and PS I of a photocatalytic reduction system), is deemed to be an ideal approach to overcome this drawback.<sup>11–13</sup> The Z-scheme photocatalytic system employs two photocatalysts (photocatalyst I for PS I and photocatalyst II for PS II) and a suitable electron transfer mediator. Photogenerated electrons within PS II combine with holes within PS I *via* the electron mediator. Thus, electrons with a high reduction ability in PS I and holes with a high oxidation ability in PS II are preserved and participate in the subsequent surface reaction. This unique advantage of powerful redox ability makes the Z-scheme system superior for water splitting and pollutant degradation. However, very limited progress in the construction of a Z-scheme system has been achieved, as it is difficult to control the desirable combination of holes and electrons *via* an electron mediator. The key point is that intimate interaction between the two photocatalysts must occur to allow the charge transfer. Up to now, some Z-scheme photocatalytic systems have been constructed for water splitting or pollutant decomposition.<sup>14–19</sup> However, the effect of contact ways (the electron mediator firstly combined with photocatalyst I or with photocatalyst II) on the Z-scheme photocatalytic performance has not been thoroughly explored.

School of Light Industry and Chemical Engineering, Dalian Polytechnic University, Dalian, China, 116034. E-mail: zhangxf010807@163.com; Fax: +86 411 86323736; Tel: +86 411 86323508

† Electronic supplementary information (ESI) available. See DOI: 10.1039/c8ra02882f

‡ These two authors contributed equally to this work.



It has been proved that bulk  $g\text{-C}_3\text{N}_4$ , as a metal-free photocatalyst with a band gap of about 2.8 eV, can eliminate organic pollutants in water and split water under visible light irradiation.<sup>20,21</sup> In 2009, Wang *et al.* first reported the use of  $g\text{-C}_3\text{N}_4$  for hydrogen or oxygen production from water splitting under visible light irradiation.<sup>22,23</sup> It is usually synthesized *via* a series of heating treatments from a simple precursor such as low-cost melamine.<sup>24</sup> The CB and VB levels of  $g\text{-C}_3\text{N}_4$  are  $-1.4$  eV and  $1.4$  eV *vs.* NHE, respectively.<sup>25</sup> So it is a promising candidate for photocatalyst I due to its relatively negative conduction band level.  $\text{FeWO}_4$  is also a visible-light-driven photocatalyst, which can decompose some pollutants *via* photocatalysis. In previous work, Kovacs *et al.* first prepared  $\text{FeWO}_4$  through a general hydrothermal method.<sup>26</sup> Gao *et al.* also reported the synthesis of  $\text{FeWO}_4$  microplates in a general low-temperature hydrothermal route.<sup>27</sup> The prepared three-dimensional  $\text{FeWO}_4$  materials displayed excellent photocatalytic activity. It is chosen as photocatalyst II because of its relatively positive valence band potential (3.2 eV *vs.* NHE). Furthermore, the band potential matching is another point to be considered for the construction of a Z-scheme photocatalytic system. That is, the conduction band potential of photocatalyst II should be more negative than that of the valence band of photocatalyst I. The conduction band potential of  $\text{FeWO}_4$  is 0.4 eV *vs.* NHE, which is more negative than that of the valence band of  $g\text{-C}_3\text{N}_4$ . RGO, a solid electron transfer medium for a Z-scheme photocatalytic system, is commonly employed for the combination of photogenerated carriers.<sup>28</sup> It is known that RGO possesses good electron transfer ability and a large surface area.<sup>29,30</sup> RGO could form tight contacts with two semiconductors and form an electron transfer bridge for Z-scheme induced charge recombination.

In this study, a new Z-scheme photocatalyst, with  $g\text{-C}_3\text{N}_4$  as photocatalyst I,  $\text{FeWO}_4$  as photocatalyst II and RGO as electron mediator was fabricated for enhanced photocatalytic ability.  $\text{RGO}/g\text{-C}_3\text{N}_4\text{-FeWO}_4$  (RGO firstly combined with  $g\text{-C}_3\text{N}_4$ ) and  $\text{RGO}/\text{FeWO}_4\text{-}g\text{-C}_3\text{N}_4$  (RGO firstly combined with  $\text{FeWO}_4$ ) were prepared to investigate the effect of the contact ways of the two photocatalysts and the electron mediator on the Z-scheme photocatalytic performance. The photocatalytic ability was evaluated by degradation of rhodamine B (RhB) under visible light.

## 2. Experimental

### 2.1 Preparation of photocatalysts

GO was synthesized from natural graphite flakes by a modified Hummers' method.<sup>31</sup> GO was dispersed in water by ultrasonication and the GO concentration was  $2 \text{ mg mL}^{-1}$ .

The  $g\text{-C}_3\text{N}_4$  was synthesized by calcination. A certain amount of melamine was put into an alumina crucible which was first heated at  $550 \text{ }^\circ\text{C}$  for 4 h with a temperature rise rate of  $10 \text{ }^\circ\text{C min}^{-1}$ . To obtain thin  $g\text{-C}_3\text{N}_4$ , the above powder was further heated at  $550 \text{ }^\circ\text{C}$  for 4 h with a temperature rise rate of  $5 \text{ }^\circ\text{C min}^{-1}$ . The resultant  $g\text{-C}_3\text{N}_4$  was collected for further use.

$\text{RGO}/\text{FeWO}_4$  was synthesized by a hydrothermal method. In the process, 0.811 g of  $\text{FeCl}_3 \cdot 6\text{H}_2\text{O}$  (3 mmol) and 0.990 g of  $\text{Na}_2\text{WO}_4 \cdot 2\text{H}_2\text{O}$  (3 mmol) were dissolved in 36 mL of deionized water. The solution was kept stirring for 2 h. Then, the prepared

GO suspension (14 mL) was dropped into the solution, and the mixture was put into an ultrasonic vibration generator for 30 min. The above mixture was then poured into a 50 mL Teflon-sealed autoclave and heated to  $180 \text{ }^\circ\text{C}$  for 8 h. After that, the precipitate was rinsed with distilled water and alcohol and collected by centrifugation. The above precipitate was dried in an oven at  $120 \text{ }^\circ\text{C}$  for 12 h. In addition, RGO or  $\text{FeWO}_4$  were fabricated by the same method without an Fe or W source or GO to serve as a control.

$\text{RGO}/g\text{-C}_3\text{N}_4$  was fabricated by a hydrothermal process. In detail, the ultra-thin  $g\text{-C}_3\text{N}_4$  (95 mg) was dispersed in 45 mL of deionized water by ultrasonication, and then a GO suspension (5 mL) was dispersed in the solution. The pH value of the above mixture was adjusted to 3.5. The above mixture was then added into a 50 mL Teflon-sealed autoclave and heated to  $180 \text{ }^\circ\text{C}$  for 8 h. After that, the precipitate was rinsed with distilled water and alcohol and collected by centrifugation. The obtained precipitate was dried in an oven at  $80 \text{ }^\circ\text{C}$  for 12 h.

$\text{FeWO}_4/g\text{-C}_3\text{N}_4$  was synthesized by a hydrothermal method. In the process, 0.811 g of  $\text{FeCl}_3 \cdot 6\text{H}_2\text{O}$  (3 mmol) and 0.990 g of  $\text{Na}_2\text{WO}_4 \cdot 2\text{H}_2\text{O}$  (3 mmol) were dissolved in 36 mL of deionized water. The solution was kept stirring for 2 h. Then, the prepared  $g\text{-C}_3\text{N}_4$  suspension was added into the solution, and the mixture was put into an ultrasonic vibration generator for 30 min. The above mixture was then poured into a 50 mL Teflon-sealed autoclave and heated to  $180 \text{ }^\circ\text{C}$  for 8 h. After that, the precipitate was rinsed with distilled water and alcohol and collected by centrifugation. The above precipitate was dried in an oven at  $120 \text{ }^\circ\text{C}$  for 12 h.

The Z-scheme photocatalyst,  $\text{RGO}/\text{FeWO}_4\text{-}g\text{-C}_3\text{N}_4$  was prepared by the following process,  $g\text{-C}_3\text{N}_4$  (100 mg) and  $\text{RGO}/\text{FeWO}_4$  (100 mg) were suspended in 50 mL of water, and then the mixture was stirred for 2 h. The precipitate was washed and dried for 5 h under the condition of  $80 \text{ }^\circ\text{C}$ . To prepare composites with identical structures (the photocatalyst combined firstly with RGO will perhaps occupy the "surface active sites" of RGO),  $\text{FeWO}_4\text{-RGO}/g\text{-C}_3\text{N}_4$  ( $\text{FeWO}_4$  and  $\text{RGO}/g\text{-C}_3\text{N}_4$ ) were prepared by the same process. And also,  $\text{FeWO}_4\text{-}g\text{-C}_3\text{N}_4$  and  $\text{RGO-FeWO}_4/g\text{-C}_3\text{N}_4$  ( $\text{RGO}$  and  $\text{FeWO}_4/g\text{-C}_3\text{N}_4$ ) were prepared by the same process as a reference.

### 2.2 Characterization

The crystal type of a sample was investigated by XRD (Rigaku, Japan) with  $\text{Cu K}\alpha$  radiation, an accelerating voltage of 40 kV, and current of 30 mA. A DRS spectrum was recorded using a UV-visible diffuse reflector (UV-2450, Shimadzu, Japan), and the wavelength range was from 200 to 800 nm. The specific surface areas (BET) of the powders were analyzed by the nitrogen adsorption-desorption method using a Micromeritics ASAP 2020 nitrogen adsorption apparatus (USA) at 77 K. PL spectra were obtained on a Fluorescence Spectrometer (LS 55, PerkinElmer, America). The morphology of the photocatalysts was observed using an optical microscope (LEICA; DM 2500M). The surface chemical bonds of the photocatalysts were investigated by XPS. The elemental composition of the synthesized materials was examined by Energy Dispersive X-ray Spectroscopy (EDX).



### 2.3 Measurement of the photocatalytic activity

Photocatalytic activity was evaluated by the degradation of RhB under visible light irradiation. A 300 W Xe lamp was employed as the light source, and the light was passed through a glass filter which could shield any light with a wavelength below 400 nm. Experiments were carried out as follows: the photocatalyst (0.08 g) was suspended in RhB solution ( $5 \text{ mg L}^{-1}$ , 80 mL). Before illumination, the suspension was stirred for 40 min in the dark to ensure the establishment of an adsorption-desorption equilibrium. A specified volume of suspension (5 mL) was collected every 20 min, and the photocatalyst was removed by centrifugation (9500 rpm, 10 min). Then, the residual RhB concentration was calculated by the absorbance of the solution at 554 nm, measured by a UV-vis spectrophotometer (Shimadzu, UV-2450). To clarify the possible oxidizing species in the photocatalytic system, EDTA, *p*-benzoquinone (BQ), and *tert*-butyl alcohol (*t*-BuOH) were employed as scavengers for holes,  $\text{O}_2^{\cdot-}$ , and  $\cdot\text{OH}$ , respectively. The concentration of the scavenger was 1 mM.

## 3. Results and discussion

### 3.1 XRD characterization

To determine the phase structure, XRD patterns were recorded. Fig. 1(a) shows the XRD patterns of GO and RGO, in which a peak was found at  $9.9^\circ$  in the GO pattern, which corresponds to (001) ( $d = 0.90 \text{ nm}$ ),<sup>32</sup> and no obvious peak was identified in the RGO pattern, indicating that the regular stacking of GO has been destroyed during the hydrothermal process. Fig. 1(b) shows the XRD patterns of  $\text{g-C}_3\text{N}_4$ ,  $\text{FeWO}_4$ ,  $\text{RGO/g-C}_3\text{N}_4$ ,  $\text{RGO/FeWO}_4$ ,  $\text{FeWO}_4\text{-g-C}_3\text{N}_4$ ,  $\text{FeWO}_4\text{-RGO/g-C}_3\text{N}_4$  and  $\text{RGO/FeWO}_4\text{-g-C}_3\text{N}_4$ .

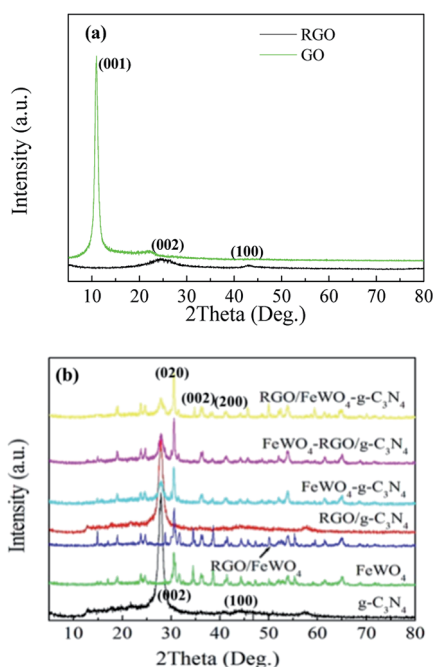


Fig. 1 XRD patterns of (a) GO and RGO, and (b)  $\text{g-C}_3\text{N}_4$ ,  $\text{FeWO}_4$ ,  $\text{RGO/FeWO}_4$ ,  $\text{FeWO}_4\text{-RGO/g-C}_3\text{N}_4$ ,  $\text{FeWO}_4\text{-g-C}_3\text{N}_4$ ,  $\text{FeWO}_4\text{-RGO/g-C}_3\text{N}_4$  and  $\text{RGO/FeWO}_4\text{-g-C}_3\text{N}_4$ .

$\text{FeWO}_4$ ,  $\text{FeWO}_4\text{-g-C}_3\text{N}_4$ ,  $\text{RGO/FeWO}_4\text{-g-C}_3\text{N}_4$  and  $\text{FeWO}_4\text{-RGO/g-C}_3\text{N}_4$ . The XRD pattern of  $\text{g-C}_3\text{N}_4$  exhibited a weak peak at  $13.01^\circ$  ( $d = 0.681 \text{ nm}$ ) and a strong peak at  $27.5^\circ$  ( $d = 0.326 \text{ nm}$ ), which can be indexed to the (002) and (100) diffraction planes of the graphite-like carbon nitride. The (002) diffraction and (100) diffraction relate to the characteristic interlayer stacking structure and the interplanar structural packing. The weak (100) diffraction indicated that the obtained  $\text{g-C}_3\text{N}_4$  was thin,<sup>33</sup> which could be attributed to the repeated exfoliation by calcination. The main reflection peaks in the  $\text{FeWO}_4$  pattern could be indexed to a monoclinic structure, according to the standard card (JCPDS-PDF, no. 27-0256).<sup>34</sup> When compositing RGO, there were no new peaks in the pattern of  $\text{RGO/g-C}_3\text{N}_4$  and  $\text{RGO/FeWO}_4$ , indicating that the introduction of RGO could not change the phase structure of  $\text{g-C}_3\text{N}_4$  or  $\text{FeWO}_4$ . A similar conclusion could be drawn based on there being no new founding peaks in the patterns of the other three compounds ( $\text{FeWO}_4\text{-g-C}_3\text{N}_4$ ,  $\text{FeWO}_4\text{-RGO/g-C}_3\text{N}_4$  and  $\text{RGO/FeWO}_4\text{-g-C}_3\text{N}_4$ ) compared with the original materials ( $\text{FeWO}_4$  and  $\text{g-C}_3\text{N}_4$ ,  $\text{FeWO}_4$  and  $\text{RGO/g-C}_3\text{N}_4$ ,  $\text{RGO/FeWO}_4$  and  $\text{g-C}_3\text{N}_4$ ). According to Scherrer's equation:  $D = k\lambda/\beta \cos \theta$ , where  $D$  is the average crystal diameter,  $k$  is a constant of value 0.89,  $\lambda$  is the radiation wavelength of 0.154 nm,  $\beta$  is the full width at half maximum of the diffraction peak, and  $\theta$  is the Bragg angle, the crystal size of  $\text{RGO/FeWO}_4\text{-g-C}_3\text{N}_4$  was 45.33 nm. Moreover, the main peaks of the original materials were all observed in the patterns of the compounds, showing that Z-scheme photocatalysts had been successfully prepared.

### 3.2 Microscope images

Fig. 2 displays the optical microscope images. In Fig. 2(a),  $\text{FeWO}_4$  shows a bone-like shape, and its size was 20–30  $\mu\text{m}$  in length and 5  $\mu\text{m}$  in width. In Fig. 2(b), some small black points were found. RGO loading on  $\text{FeWO}_4$  made the particle image darker. Compared with single  $\text{FeWO}_4$ , the particle size of  $\text{FeWO}_4$  in  $\text{RGO/FeWO}_4$  (below 10  $\mu\text{m}$ ) was obviously reduced. The exact reason was not clear, but it can be speculated that RGO was a model which restricted the growth of  $\text{FeWO}_4$  particles. As shown in Fig. 2(c),  $\text{g-C}_3\text{N}_4$  was flaky. The image becomes

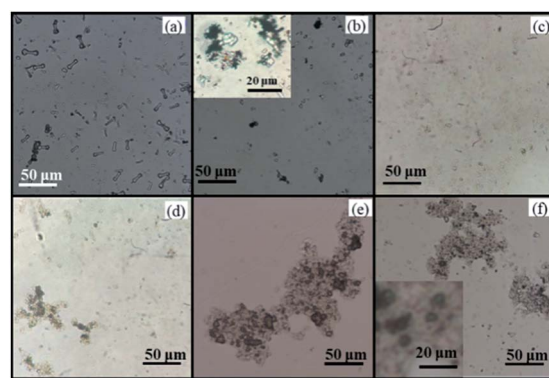


Fig. 2 Optical microscope images of  $\text{FeWO}_4$  (a),  $\text{RGO/FeWO}_4$  (b),  $\text{g-C}_3\text{N}_4$  (c),  $\text{RGO/g-C}_3\text{N}_4$  (d),  $\text{FeWO}_4\text{-RGO/g-C}_3\text{N}_4$  (e) and  $\text{RGO/FeWO}_4\text{-g-C}_3\text{N}_4$  (f).



**Table 1** Specific surface areas of g-C<sub>3</sub>N<sub>4</sub>, FeWO<sub>4</sub>, RGO/g-C<sub>3</sub>N<sub>4</sub>, RGO/FeWO<sub>4</sub>, FeWO<sub>4</sub>-g-C<sub>3</sub>N<sub>4</sub>, RGO/FeWO<sub>4</sub>-g-C<sub>3</sub>N<sub>4</sub> and FeWO<sub>4</sub>-RGO/g-C<sub>3</sub>N<sub>4</sub> from N<sub>2</sub> adsorption/desorption

Sample	RGO	FeWO <sub>4</sub>	RGO/FeWO <sub>4</sub>	g-C <sub>3</sub> N <sub>4</sub>	RGO/g-C <sub>3</sub> N <sub>4</sub>	FeWO <sub>4</sub> -g-C <sub>3</sub> N <sub>4</sub>	FeWO <sub>4</sub> -RGO/g-C <sub>3</sub> N <sub>4</sub>	RGO/FeWO <sub>4</sub> -g-C <sub>3</sub> N <sub>4</sub>
BET (m <sup>2</sup> g <sup>-1</sup> )	178.5	24.8	38.4	86.7	83.9	75.6	75.3	75.3

lighter, which could be attributed to good light transmission by thin C<sub>3</sub>N<sub>4</sub>. A darker image was found in Fig. 2(d), indicating that RGO and g-C<sub>3</sub>N<sub>4</sub> were successfully hybridized. In Fig. 2(e), it was found that RGO/g-C<sub>3</sub>N<sub>4</sub> was successfully and uniformly loaded onto FeWO<sub>4</sub> particles. From Fig. 2(f), g-C<sub>3</sub>N<sub>4</sub> was successfully loaded onto RGO/FeWO<sub>4</sub> particles, and maintained a uniformity of distribution, which could promote charge transfer between the materials. The elemental composition of the different synthesized materials was examined by EDX. As shown in Table S1,<sup>†</sup> RGO/FeWO<sub>4</sub>-g-C<sub>3</sub>N<sub>4</sub> and FeWO<sub>4</sub>-RGO/g-C<sub>3</sub>N<sub>4</sub> are composed of C, N, O, Fe and W. Compared with the weight ratio of C/N in g-C<sub>3</sub>N<sub>4</sub> (0.64), the weight ratios of C/N in RGO/FeWO<sub>4</sub>-g-C<sub>3</sub>N<sub>4</sub> (0.76) and FeWO<sub>4</sub>-RGO/g-C<sub>3</sub>N<sub>4</sub> (0.81) are higher. This means that RGO has been successfully introduced.

### 3.3 BET

The specific surface area is an important parameter for photocatalysts, because photocatalysis mainly occurs on and near the surface of photocatalysts. The specific surface area was determined by N<sub>2</sub> adsorption/desorption, and the calculated values are displayed in Table 1. It can be seen from Table 1 that the specific surface area of FeWO<sub>4</sub> was 24.8 m<sup>2</sup> g<sup>-1</sup>. After coupling with RGO, the BET value of FeWO<sub>4</sub>/RGO increased (38.4 m<sup>2</sup> g<sup>-1</sup>), which could be ascribed to the large specific surface area of RGO and the decreased particle size of FeWO<sub>4</sub>. Due to its thin layer structure, g-C<sub>3</sub>N<sub>4</sub> possessed a large surface area (86.7 m<sup>2</sup> g<sup>-1</sup>). Compared with that of g-C<sub>3</sub>N<sub>4</sub>, the specific surface area of RGO/g-C<sub>3</sub>N<sub>4</sub> (83.9 m<sup>2</sup> g<sup>-1</sup>) did not obviously change because of the similar specific surface areas of RGO and g-C<sub>3</sub>N<sub>4</sub>. Table 1 also shows that RGO/FeWO<sub>4</sub>-g-C<sub>3</sub>N<sub>4</sub> and FeWO<sub>4</sub>-RGO/g-C<sub>3</sub>N<sub>4</sub> had similar specific surface areas.

### 3.4 XPS

To discover the surface chemical bonds of the photocatalysts, XPS was recorded and the results are shown in Fig. 3. The Fe 2p spectrum of FeWO<sub>4</sub> exhibited one peak (710.0 eV), and no obvious shift in peaks was found in the spectra of RGO/FeWO<sub>4</sub> or RGO/FeWO<sub>4</sub>-C<sub>3</sub>N<sub>4</sub>. However, in the W 4f spectra, higher binding energies of RGO/FeWO<sub>4</sub> and RGO/FeWO<sub>4</sub>-C<sub>3</sub>N<sub>4</sub> (35.0 eV and 37.1 eV) were determined compared with those of FeWO<sub>4</sub> (34.6 and 36.7 eV). The XPS results first revealed that the chemical environment of W was changed after RGO coupling, which could be attributed to the generation of chemical bonds between RGO and FeWO<sub>4</sub> during the hydrothermal process. A similar result was also found in other literature.<sup>34</sup> Furthermore, no new chemical bonds were generated during C<sub>3</sub>N<sub>4</sub> loading onto RGO/FeWO<sub>4</sub> by physical mixing. The peak found in the C 1s spectrum of C<sub>3</sub>N<sub>4</sub> centered at 284.6 eV was attributed to the C-C bond of contaminated carbon. The peak at 288.0 eV corresponds to the tertiary carbon C-N<sub>3</sub>.<sup>35</sup> There was no obvious

shift in the peaks of RGO/C<sub>3</sub>N<sub>4</sub> and RGO/C<sub>3</sub>N<sub>4</sub>-FeWO<sub>4</sub>, indicating there was no new generation of chemical bonds between RGO and C<sub>3</sub>N<sub>4</sub> in RGO/C<sub>3</sub>N<sub>4</sub> or RGO/C<sub>3</sub>N<sub>4</sub>-FeWO<sub>4</sub>.

### 3.5 DRS

DRS and band gap calculations are illustrated in Fig. 4. Both samples of g-C<sub>3</sub>N<sub>4</sub> and FeWO<sub>4</sub> exhibited significant absorption in the visible light region. The band gaps calculated by the Kubelka-Munk function of g-C<sub>3</sub>N<sub>4</sub> and FeWO<sub>4</sub> were 2.85 and 2.81 eV, respectively, which were similar to the reported values.<sup>27,29</sup> RGO/FeWO<sub>4</sub>-g-C<sub>3</sub>N<sub>4</sub> and FeWO<sub>4</sub>-RGO/g-C<sub>3</sub>N<sub>4</sub> showed enhanced absorption intensity compared with C<sub>3</sub>N<sub>4</sub> and FeWO<sub>4</sub>, especially in the range of 400-800 nm. It was speculated that the dark color of the powders made them absorb more photons.

### 3.6 PL spectra

PL spectra analysis was used to discover the separation efficiency of photogenerated charge carriers in semiconductors. A larger PL intensity means more recombination of photogenerated charge pairs. In the detected PL spectra (Fig. 5), the intensity of RGO/g-C<sub>3</sub>N<sub>4</sub>-FeWO<sub>4</sub> was lower than that of RGO/g-C<sub>3</sub>N<sub>4</sub>, and the intensity of RGO/g-C<sub>3</sub>N<sub>4</sub> was smaller than that of g-C<sub>3</sub>N<sub>4</sub>. The result indicated that loading RGO onto g-C<sub>3</sub>N<sub>4</sub> could improve the separation performance of photogenerated charge carriers, caused by the migration of photogenerated electrons from g-C<sub>3</sub>N<sub>4</sub> to RGO. The lowest PL intensity of RGO/g-C<sub>3</sub>N<sub>4</sub>-FeWO<sub>4</sub> indicated that the separation of photogenerated charge carriers could be improved through the construction of a Z-scheme system. A similar conclusion could be reached by comparing the PL intensity with FeWO<sub>4</sub>, RGO/FeWO<sub>4</sub> and RGO/FeWO<sub>4</sub>-g-C<sub>3</sub>N<sub>4</sub>, which further confirmed the enhanced

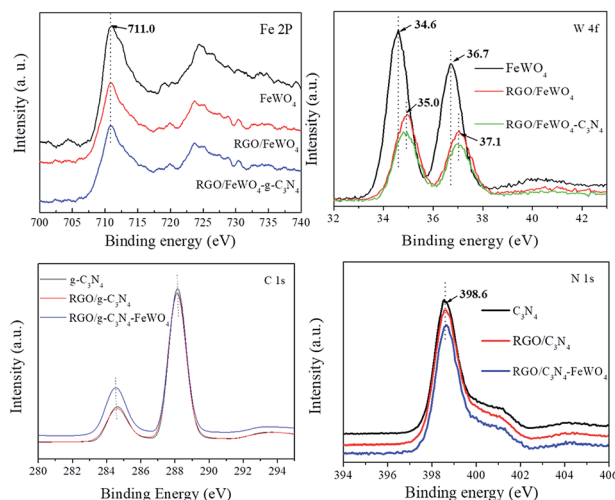


**Fig. 3** XPS spectra of Fe 2P, W 4f, C 1s and N 1s.



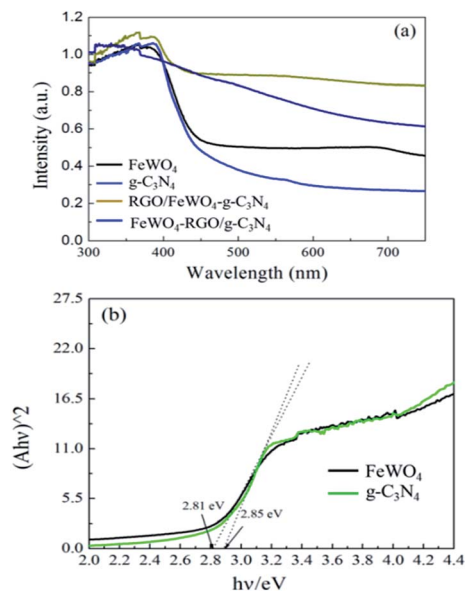


Fig. 4 (a) DRS and (b) band gap calculation by the Kubelka–Munk function of  $\text{FeWO}_4$ ,  $\text{g-C}_3\text{N}_4$ ,  $\text{FeWO}_4\text{-RGO/g-C}_3\text{N}_4$  and  $\text{RGO/FeWO}_4\text{-g-C}_3\text{N}_4$ .

separation of photogenerated charge carriers in the Z-scheme photocatalyst. With respect to a comparison of  $\text{RGO/g-C}_3\text{N}_4\text{-FeWO}_4$  and  $\text{RGO/FeWO}_4\text{-g-C}_3\text{N}_4$ , the PL intensity of  $\text{RGO/FeWO}_4\text{-g-C}_3\text{N}_4$  was slightly lower, indicating that the separation of photogenerated charge carriers on it was more effective. Since less recombination of photogenerated charge carriers leads to better photocatalytic efficiency, it could be expected that the Z-scheme photocatalyst would have high photocatalytic ability, and  $\text{RGO/FeWO}_4\text{-g-C}_3\text{N}_4$  would have the highest photocatalytic performance.

### 3.7 Photocatalytic activity

The photocatalytic performances of the photocatalysts were evaluated through RhB degradation under visible light irradiation, and the results are shown in Fig. 6. From Fig. 6(a), before light irradiation, only 7.4% of RhB was removed on  $\text{FeWO}_4$  after 20 min, meaning that the adsorption of RhB on  $\text{FeWO}_4$  was poor. After RGO loading, 23.9% of RhB with  $\text{g-C}_3\text{N}_4$  was removed, which could be attributed to the large specific surface area of

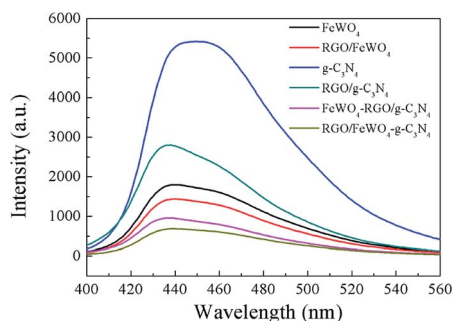


Fig. 5 PL spectra of  $\text{FeWO}_4$ ,  $\text{RGO/FeWO}_4$ ,  $\text{g-C}_3\text{N}_4$ ,  $\text{RGO/g-C}_3\text{N}_4$ ,  $\text{FeWO}_4\text{-RGO/g-C}_3\text{N}_4$  and  $\text{RGO/FeWO}_4\text{-g-C}_3\text{N}_4$ .

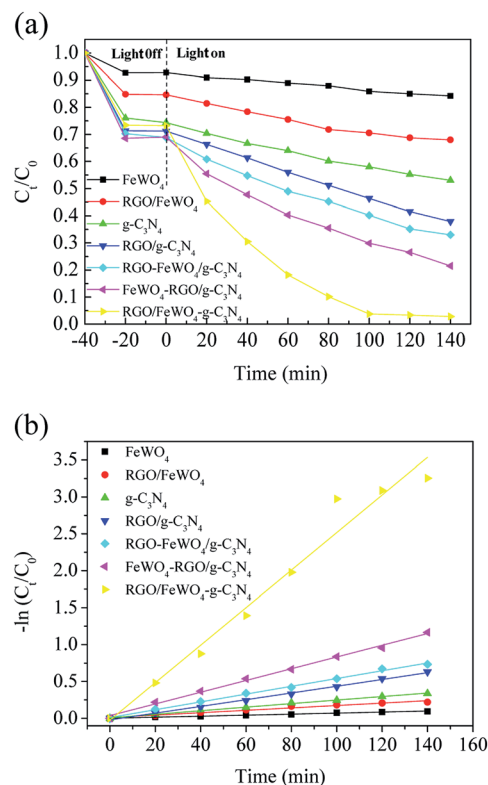


Fig. 6 (a)  $C_t/C_0$  versus reaction time and (b) the kinetic curves for photocatalytic degradation of RhB on  $\text{FeWO}_4$ ,  $\text{RGO/FeWO}_4$ ,  $\text{g-C}_3\text{N}_4$ ,  $\text{RGO/g-C}_3\text{N}_4$ ,  $\text{FeWO}_4\text{-g-C}_3\text{N}_4$ ,  $\text{FeWO}_4\text{-RGO/g-C}_3\text{N}_4$  and  $\text{RGO/FeWO}_4\text{-g-C}_3\text{N}_4$  under visible light irradiation.

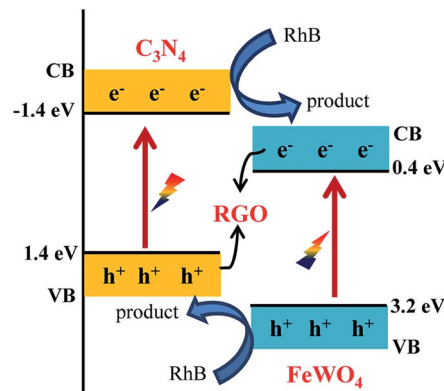
$\text{RGO}$ . RhB removal on  $\text{RGO/g-C}_3\text{N}_4$  was slightly improved compared with that on  $\text{g-C}_3\text{N}_4$ , which is possibly attributed to the small difference between the specific surface areas of  $\text{g-C}_3\text{N}_4$  and  $\text{RGO/g-C}_3\text{N}_4$ . The RhB removals on  $\text{FeWO}_4\text{-g-C}_3\text{N}_4$ ,  $\text{FeWO}_4\text{-RGO/g-C}_3\text{N}_4$  and  $\text{RGO/FeWO}_4\text{-g-C}_3\text{N}_4$  were similar to that of  $\text{RGO/g-C}_3\text{N}_4$ . After visible light illumination for 120 min, about 15.0% of RhB was removed in the presence of  $\text{FeWO}_4$ , and the removal on  $\text{g-C}_3\text{N}_4$  was 31.2%, indicating that  $\text{FeWO}_4$  and  $\text{g-C}_3\text{N}_4$  could be excited by visible light and could degrade RhB in a photocatalytic process. After RGO hybridisation, under the same reaction conditions, the removals of RhB on  $\text{RGO/FeWO}_4$  and  $\text{RGO/g-C}_3\text{N}_4$  were 32.1% and 58.4%, respectively. The enhanced photocatalytic ability could be attributed to the improved separation of photogenerated charge carriers of  $\text{RGO/FeWO}_4$  and  $\text{RGO/g-C}_3\text{N}_4$ .

RhB removals by  $\text{FeWO}_4\text{-RGO/g-C}_3\text{N}_4$  and  $\text{RGO/FeWO}_4\text{-g-C}_3\text{N}_4$  were 73.5% and 92.3%, respectively, which were higher than those of previously mentioned photocatalysts, certifying that a Z-scheme structure could boost the photocatalytic efficiency. To further confirm the Z-scheme effect, the photocatalytic ability of  $\text{FeWO}_4\text{-g-C}_3\text{N}_4$  and  $\text{RGO/FeWO}_4\text{-g-C}_3\text{N}_4$ , which had the same amounts of  $\text{g-C}_3\text{N}_4$ ,  $\text{FeWO}_4$  and  $\text{RGO}$  to those of  $\text{FeWO}_4\text{-RGO/g-C}_3\text{N}_4$  and  $\text{RGO/FeWO}_4\text{-g-C}_3\text{N}_4$  was evaluated as a reference. Under the same conditions, the RhB removal rates were significantly lower than those of  $\text{FeWO}_4\text{-RGO/g-C}_3\text{N}_4$  and  $\text{RGO/FeWO}_4\text{-g-C}_3\text{N}_4$ , confirming that the enhanced photocatalytic performance of  $\text{FeWO}_4\text{-RGO/g-C}_3\text{N}_4$



and RGO/FeWO<sub>4</sub>-g-C<sub>3</sub>N<sub>4</sub> was owing to the Z-scheme effect. The photocatalytic ability of RGO/FeWO<sub>4</sub>-g-C<sub>3</sub>N<sub>4</sub> was higher than that of FeWO<sub>4</sub>-RGO/g-C<sub>3</sub>N<sub>4</sub>, suggesting that the contact ways (the electron mediator firstly combined with photocatalyst I or with photocatalyst II) could affect the Z-scheme photocatalytic performance. The photocatalytic process is fitted well with a pseudo-first-order reaction, and the kinetic curves of RhB degradation are depicted in Fig. 6(b). The kinetic constants of RhB degradation on FeWO<sub>4</sub>, RGO/FeWO<sub>4</sub>, g-C<sub>3</sub>N<sub>4</sub>, RGO/g-C<sub>3</sub>N<sub>4</sub>, RGO-FeWO<sub>4</sub>/g-C<sub>3</sub>N<sub>4</sub>, FeWO<sub>4</sub>-RGO/g-C<sub>3</sub>N<sub>4</sub> and RGO/FeWO<sub>4</sub>-g-C<sub>3</sub>N<sub>4</sub> were calculated to be 0.00069, 0.0016, 0.0024, 0.0046, 0.0053, 0.0080 and 0.025 min<sup>-1</sup>, respectively. To elucidate the influence of RGO on the photocatalytic performance of RGO/FeWO<sub>4</sub>-g-C<sub>3</sub>N<sub>4</sub>, the RGO content in RGO/FeWO<sub>4</sub>-g-C<sub>3</sub>N<sub>4</sub> was regulated. The results showed that RGO/FeWO<sub>4</sub>-g-C<sub>3</sub>N<sub>4</sub> with the addition of 14 mg of RGO showed the best performance. The detailed information is displayed in Fig. S1.† The stability of g-C<sub>3</sub>N<sub>4</sub>-RGO/FeWO<sub>4</sub> for the photocatalytic degradation of RhB was tested, as shown in Fig. 7. The photocatalytic activity of g-C<sub>3</sub>N<sub>4</sub>-RGO/FeWO<sub>4</sub> shows almost no change after 5 recycling runs, and the RhB removal was maintained at above 90%. This result suggests that g-C<sub>3</sub>N<sub>4</sub>-RGO/FeWO<sub>4</sub> possesses good stability and recyclability, which are significant for practical applications.

The reason for the improved photocatalytic performance was not exactly clear. It may be caused by the decreased FeWO<sub>4</sub> particle size in RGO/FeWO<sub>4</sub>-g-C<sub>3</sub>N<sub>4</sub>, or the force deference of chemical bond (RGO and FeWO<sub>4</sub> in RGO/FeWO<sub>4</sub>-g-C<sub>3</sub>N<sub>4</sub>) and physical contact (RGO and g-C<sub>3</sub>N<sub>4</sub> in FeWO<sub>4</sub>-RGO/g-C<sub>3</sub>N<sub>4</sub>). A possible mechanism for RhB degradation with RGO/FeWO<sub>4</sub>-g-C<sub>3</sub>N<sub>4</sub> as the photocatalyst was proposed and is shown in Scheme 1. When irradiated, the g-C<sub>3</sub>N<sub>4</sub> and FeWO<sub>4</sub> particles were excited and generated electrons and holes. Due to the match of the band positions, photogenerated electrons in FeWO<sub>4</sub> would combine with holes in g-C<sub>3</sub>N<sub>4</sub> through RGO (the electron mediator). The photogenerated holes in FeWO<sub>4</sub> and photogenerated electrons in g-C<sub>3</sub>N<sub>4</sub> were spatially separated. Thus, the separation of photogenerated holes and electrons was enhanced, and more electrons and holes would participate in the oxidation reaction. Meanwhile, remaining holes (on the VB of FeWO<sub>4</sub>) and electrons (on the CB of the g-C<sub>3</sub>N<sub>4</sub>) would



Scheme 1 Proposed mechanism of enhanced photocatalytic ability of RGO/FeWO<sub>4</sub>-g-C<sub>3</sub>N<sub>4</sub>.

promote the photocatalytic degradation of RhB because of its powerful oxidation ability and excellent reduction performance.

To further clarify the possible oxidizing species in the photocatalytic system, a radical quenching experiment was performed. In this experiment, EDTA, *p*-benzoquinone (BQ), and *tert*-butyl alcohol (*t*-BuOH) were employed as scavengers for holes, O<sub>2</sub><sup>•-</sup>, and •OH, respectively. Fig. S2a† shows that the photocatalytic efficiency decreased after introducing EDTA and BQ, with the kinetic constant of RhB degradation decreasing from 0.025 min<sup>-1</sup> to 0.020 min<sup>-1</sup> and 0.017 min<sup>-1</sup>, respectively (Fig. S2b†), meaning the holes and O<sub>2</sub><sup>•-</sup> participated in the RhB oxidation. When *t*-BuOH was added, the decrease in performance was more significant. The kinetic constant of RhB degradation decreased to 0.0084 min<sup>-1</sup>, suggesting that •OH was the major oxidant in the photocatalytic system.

## 4. Conclusions

Z-scheme photocatalysts, in which g-C<sub>3</sub>N<sub>4</sub>, FeWO<sub>4</sub> and RGO served as photocatalyst I, photocatalyst II and electron mediator, respectively, were successfully fabricated. The photocatalytic degradation rate of RhB was largely enhanced by the construction of a Z-scheme photocatalyst. The contact ways (the electron mediator firstly combined with photocatalyst I or with photocatalyst II) could influence the photocatalytic ability of the Z-scheme photocatalyst. The enhanced photocatalytic performance was attributed to the Z-scheme effect induced efficient separation of photogenerated electrons and holes. Furthermore, accumulated holes (on the VB of FeWO<sub>4</sub>) with powerful oxidation ability and remaining electrons (on the CB of the g-C<sub>3</sub>N<sub>4</sub>) with excellent reduction ability would promote the photocatalytic degradation of RhB. It was rationally confirmed that constructing a Z-scheme photocatalyst was a versatile method to explore a high performance photocatalyst, and the Z-scheme photocatalytic performance could be controlled by the contact ways.

## Conflicts of interest

There are no conflicts to declare.

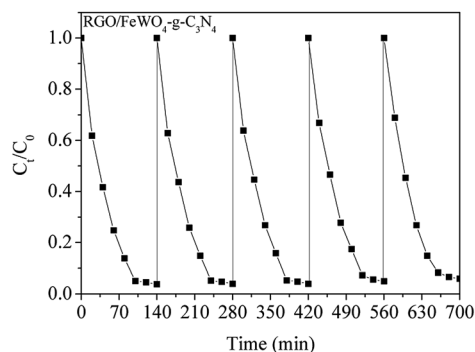


Fig. 7 The stability of RGO/FeWO<sub>4</sub>-g-C<sub>3</sub>N<sub>4</sub> for photocatalytic degradation of RhB under visible light illumination.



## Acknowledgements

This work was supported by the National Science Fund of China (Project No. 21577008) and Fundamental Research Funds for Central Universities (Project No. 2016J004).

## References

- M. Li, C. Feng, W. Hu, Z. Zhang and N. Sugiur, Electrochemical degradation of phenol using electrodes of Ti/RuO<sub>2</sub>-Pt and Ti/IrO<sub>2</sub>-Pt, *J. Hazard. Mater.*, 2009, **162**, 455–462.
- S. Girish Kumar and K. S. R. Koteswara Rao, Tungsten-based nanomaterials (WO<sub>3</sub> & Bi<sub>2</sub>WO<sub>6</sub>): modifications related to charge carrier transfer mechanisms and photocatalytic applications, *Appl. Surf. Sci.*, 2015, **355**, 939–958.
- X. Quan, S. Yang, X. Ruan and H. Zhao, Preparation of titania nanotubes and their environmental applications as electrode, *Environ. Sci. Technol.*, 2005, **39**, 3770–3775.
- J. Hu, L. Ren, Y. Guo, H. Liang, A. Cao, L. Wan and C. Bai, Mass production and high photocatalytic activity of ZnS nanoporous nanoparticles, *Angew. Chem., Int. Ed.*, 2005, **44**, 1269–1273.
- M. Tabata, K. Maeda, M. Higashi, D. Lu, T. Takata, R. Abe and K. Domen, Modified Ta<sub>3</sub>N<sub>5</sub> powder as a photocatalyst for O<sub>2</sub> evolution in a two-step water splitting system with an iodate/iodide shuttle redox mediator under visible light, *Langmuir*, 2010, **26**, 9161–9165.
- D. Wang, T. Kako and J. Ye, Efficient photocatalytic decomposition of acetaldehyde over a solid-solution perovskite (Ag<sub>0.75</sub>Sr<sub>0.25</sub>)(Nb<sub>0.75</sub>Ti<sub>0.25</sub>)O<sub>3</sub> under visible-light irradiation, *J. Am. Chem. Soc.*, 2008, **130**, 2724–2725.
- P. Madhusudan, J. Ran, J. Zhang, J. Yu and G. Liu, Novel urea assisted hydrothermal synthesis of hierarchical BiVO<sub>4</sub>/Bi<sub>2</sub>O<sub>2</sub>CO<sub>3</sub> nanocomposites with enhanced visible-light photocatalytic activity, *Appl. Catal., B*, 2011, **110**, 286–295.
- L. Konga, Z. Jiang, H. H. Lai, R. J. Nicholls, T. Xiao, M. O. Jones and P. P. Edwards, Unusual reactivity of visible-light-responsive AgBr–BiOBr heterojunction photocatalysts, *J. Catal.*, 2012, **293**, 116–125.
- W. Zhang, Y. Li, C. Wang and P. Wang, Kinetics of heterogeneous photocatalytic degradation of rhodamine B by TiO<sub>2</sub>-coated activated carbon: Roles of TiO<sub>2</sub> content and light intensity, *Desalination*, 2011, **266**, 40–45.
- J. Luo, Y. Wang, D. Cao, K. Xiao, T. Guo and X. Zhao, Enhanced photoelectrocatalytic degradation of 2, 4-dichlorophenol by TiO<sub>2</sub>/Ru–IrO<sub>2</sub> bifacial electrode, *Chem. Eng. J.*, 2018, **343**, 69–77.
- K. Iwashina, A. Iwase, Y. H. Ng, R. Amal and A. Kudo, Z-Schematic water splitting into H<sub>2</sub> and O<sub>2</sub> using metal sulfide as a hydrogen-evolving photocatalyst and reduced graphene oxide as a solid-state electron mediator, *J. Am. Chem. Soc.*, 2015, **137**, 604–607.
- Q. Jia, A. Iwase and A. Kudo, BiVO<sub>4</sub>-Ru/SrTiO<sub>3</sub>: Rh composite Z-scheme photocatalyst for solar water splitting, *Chem. Sci.*, 2014, **5**, 1513.
- H. Katsumata, Y. Tachi, T. Suzuki and S. Kaneco, Z-scheme photocatalytic hydrogen production over WO<sub>3</sub>/g-C<sub>3</sub>N<sub>4</sub> composite photocatalysts, *RSC Adv.*, 2014, **4**, 21405.
- H. Li, X. Quan, S. Chen and H. Yu, Ferroelectric-enhanced Z-schematic electron transfer in BiVO<sub>4</sub>-BiFeO<sub>3</sub>-CuInS<sub>2</sub> for efficient photocatalytic pollutant degradation, *Appl. Catal., B*, 2017, **209**, 591–599.
- Y. Gong, X. Quan, H. Yu and S. Chen, Synthesis of Z-scheme Ag<sub>2</sub>CrO<sub>4</sub>/Ag/g-C<sub>3</sub>N<sub>4</sub> composite with enhanced visible-light photocatalytic activity for 2,4-dichlorophenol, *Appl. Catal., B*, 2017, **219**, 439–449.
- H. Tada, T. Mitsui, T. Kiyonaga, T. Akita and K. Tanaka, All-solid-state Z-scheme is CdS-Au-TiO<sub>2</sub> three-component nanojunction system, *Nat. Mater.*, 2006, **5**, 782–786.
- W. K. Jo, T. Adinaveen, J. J. Vijaya and N. C. S. Selvam, Synthesis of MoS<sub>2</sub> nanosheet supported Z-scheme TiO<sub>2</sub>/g-C<sub>3</sub>N<sub>4</sub> photocatalysts for the enhanced photocatalytic degradation of organic water pollutants, *RSC Adv.*, 2016, **6**, 10487–10497.
- F. Wu, X. Li, W. Liu and S. Zhang, Highly enhanced photocatalytic degradation of methylene blue over the indirect all-solid-state Z-scheme g-C<sub>3</sub>N<sub>4</sub>-RGO-TiO<sub>2</sub> nanoheterojunctions, *Appl. Surf. Sci.*, 2017, **405**, 60–70.
- W. Jo and N. C. S. Selvam, Z-scheme CdS/g-C<sub>3</sub>N<sub>4</sub> composites with RGO as an electron mediator for efficient photocatalytic H<sub>2</sub> production and pollutant degradation, *Chem. Eng. J.*, 2017, **317**, 913–924.
- M. Ye, Z. Zhao, Z. Hu, L. Liu, H. Ji, Z. Shen and T. Ma, 0D/2D Heterojunctions of vanadate quantum dots/graphitic carbon nitride nanosheets for enhanced visible-light-driven photocatalysis, *Angew. Chem.*, 2017, **56**, 8407–8411.
- H. Li, Y. Sun, Z. Y. Yuan, Y. Zhu and T. Ma, Titanium Phosphonate Based Metal-Organic Frameworks with Hierarchical Porosity for Enhanced Photocatalytic Hydrogen Evolution, *Angew. Chem.*, 2018, **57**, 3222–3227.
- X. Wang, K. Maeda, A. Thomas, K. Takanabe, G. Xin, J. M. Carlsson, K. Domen and M. Antonietti, A metal-free polymeric photocatalyst for hydrogen production from water under visible light, *Nat. Mater.*, 2009, **8**, 76–80.
- K. Maeda, X. Wang, Y. Nishihara, D. Lu, M. Antonietti and K. Domen, Photocatalytic activities of graphitic carbon nitride powder for water reduction and oxidation under visible light, *J. Phys. Chem. C*, 2009, **113**, 4940–4947.
- S. C. Yan, Z. S. Li and Z. G. Zou, Photodegradation performance of g-C<sub>3</sub>N<sub>4</sub> fabricated by directly heating melamine, *Langmuir*, 2009, **25**, 10397–10401.
- S. Chu, Y. Wang, Y. Guo, J. Feng, C. Wang, W. Luo, X. Fan and Z. Zou, Band structure engineering of carbon nitride: In search of a polymer photocatalyst with high photooxidation property, *ACS Catal.*, 2013, **3**, 912–919.
- T. N. Kovacs, G. Pokol, F. Gaber, D. Nagy, T. Igricz, I. E. Lukacs, Z. Fogarassy, K. Balazsi and I. M. Szilagyi, Preparation of iron tungstate (FeWO<sub>4</sub>) nanosheets by hydrothermal method, *Mater. Res. Bull.*, 2017, **95**, 563–569.
- Q. Gao and Z. Liu, FeWO<sub>4</sub> nanorods with excellent UV-visible light photocatalysis, *Prog. Nat. Sci.: Mater. Int.*, 2017, **27**, 556–560.



- 28 A. Iwase, Y. H. Ng, Y. Ishiguro, A. Kudo and R. Amal, Reduced graphene oxide as a solid-state electron mediator in Z-scheme photocatalytic water splitting under visible light, *J. Am. Chem. Soc.*, 2011, **133**, 11054–11057.
- 29 A. Iwase, Y. H. Ng, Y. Ishiguro, A. Kudo and R. Amal, Reduced graphene oxide as a solid-state electron mediator in Z-scheme photocatalytic water splitting under visible light, *J. Am. Chem. Soc.*, 2011, **133**, 11054–11057.
- 30 F. Wu, X. Li, W. Liu and S. Zhang, Highly enhanced photocatalytic degradation of methylene blue over the indirect all-solid-state Z-scheme g-C<sub>3</sub>N<sub>4</sub>-RGO-TiO<sub>2</sub> nanoheterojunctions, *Appl. Surf. Sci.*, 2017, **405**, 60–70.
- 31 W. S. Hummels Jr and R. E. Offeman, Preparation of Graphitic oxide, *J. Am. Chem. Soc.*, 1958, **80**, 1339.
- 32 Q. Xiang, J. Yu and M. Jaroniec, Preparation and enhanced visible-light photocatalytic H<sub>2</sub>-production activity of graphene/C<sub>3</sub>N<sub>4</sub> composites, *J. Phys. Chem. C*, 2011, **115**, 7355–7363.
- 33 J. Xu, L. W. Zhang, R. Shi and Y. F. Zhu, Chemical exfoliation of graphitic carbon nitride for efficient heterogeneous photocatalysis, *J. Mater. Chem. A*, 2013, **1**, 14766–14772.
- 34 S. Li, G. Dong, R. Hailili, L. Yang, Y. Li, F. Wang, Y. Zeng and C. Wang, Effective photocatalytic H<sub>2</sub>O<sub>2</sub> production under visible light irradiation at g-C<sub>3</sub>N<sub>4</sub> modulated by carbon vacancies, *Appl. Catal., B*, 2016, **190**, 26–35.
- 35 G. He, M. Chen, Y. Liu, X. Li and Y. Ju, Hydrothermal synthesis of FeWO<sub>4</sub>-graphene composites and their photocatalytic activities under visible light, *Appl. Surf. Sci.*, 2015, **351**, 474–479.

